PROCEEDINGS OF ECOS 2023 - THE 36TH INTERNATIONAL CONFERENCE ON
EFFICIENCY, COST, OPTIMIZATION, SIMULATION AND ENVIRONMENTAL IMPACT OF ENERGY SYSTEMS
25-30 JUNE 2023, LAS PALMAS DE GRAN CANARIA, SPAIN

Preliminary design guidelines for a vortex-based energy harvester for water flows

Francesco De Vanna[a], Alberto Benato[b, (CA)], and Giovanna Cavazzini[c]

[a] *Department of Industrial Engineering - University of Padova, Padova, Italy, francesco.devanna@unipd.it*
[b] *Department of Industrial Engineering - University of Padova, Padova, Italy, alberto.benato@unipd.it (CA)*
[c] *Department of Industrial Engineering - University of Padova, Padova, Italy, giovanna.cavazzini@unipd.it*

Abstract:
The proposed study presents preliminary design guidelines for vortex-induced vibration energy harvesting devices. In particular, this study combines high-quality computational fluid dynamics techniques to systematically examine the oscillatory behaviour of flow-induced vibration cylinders in cross-flow configurations. Simple cylinders are examined and modelled in terms of masses, damping, and stiffness. The design maps are derived after a comprehensive validation of the numerical model. The maps link the most important flow characteristics at which the device should be installed to the foundational variables relevant to energy recovery and the most important flow properties on which the device must be installed. The results show that the lock-in conditions are achieved with a reduced velocity value of about 5. Additionally, the analysis revealed that the density ratio is a key design parameter, since the functional properties of the device are ensured only for modest values, roughly around 10. In essence, the results provide significant insights into the fluid mechanics of the system, direct indications of the nondimensional groups that regulate system physics, and practical tips for its design.

Keywords:
vortex-induced vibrations, energy harvesting, mini-hydro, virtual design.

1. Introduction

Since the beginning of civilisation, the harvesting of energy from waterways has played a fundamental role in the implementation of human society. In fact, water flows are generally easily accessible and provide a constant energy supply to help with several human activities. However, today, the scientific community recognises that the most profitable water resources for electricity generation have already been fully exploited with standard and well-established technologies. Therefore, novel and disruptive ideas are needed in the hydroelectric landscape. In particular, the mini-hydro aims to generate electricity from tiny/minimal water sources using innovative concepts. These prototypes are a long way different from canonical turbine/watermill plants, the latter requiring significant financial investments and long payback periods. Thus, in a world that is moving from fossil to renewable resources and from concentrate to distributed generation, mini- and microhydro technologies will play a crucial role, especially if the new devices/systems will generate electricity from untapped water flows in an appealing way for building, industrial, and tertiary sectors.

One of the most relevant innovations in this field is related to energy harvesters. Generally speaking, these devices consist of electrofluid-mechanical systems designed to convert the energy content of water flowing into pipes, canals, and conduits into electricity, mainly inducing a vibration on a bluff body linked to an electric generator. In this context, in-depth study and understanding of the Vortex-Induced Vibration (VIV) phenomenon become fundamental, especially concerning its application to energy harvesting systems. Therefore, several studies have made great progress in understanding the causes and characteristics of VIV. This need comes from the fact that vibrations induced by fluid flows on bluff bodies can be particularly dangerous in many engineering situations, such as projects that involve bridges, offshore structures, and cables, in particular if the lock-in state is reached. However, vibrations can also be seen as an energy source and can be used for energy production.

In particular, from the pioneering work of Goswami et al. [1], which presented the experimental results of the properties of the vortex-induced response of a spring-mounted circular cylinder in a low-speed wind tunnel, several other contributions appeared in the literature. Blackburn and Henderson [2], for instance, addressed the free vibration behaviour and wake models in vortex-induced and free oscillations through a numerical model, showing that the method is a valid alternative to experimental setups. Later on, Zhao et al. [3], investigated the steady and oscillatory flow of VIV systems by numerically solving the two-dimensional Reynolds-Averaged Navier-Stokes (RANS) equations. The main finding is that the combination of steady flow and oscillatory pattern widens the lock-in regime, achieving a twice broader lock-in regime concerning the pure steady or pure

https://doi.org/10.52202/069564-0052

oscillatory flow.

The works mentioned above can be considered to be the foundation of VIV fundamental physics, while the use of VIV systems to harvest energy became a hot research topic only in recent years. In particular, the idea at the base of energy harvesting with VIV systems refers to the combination of bluff bodies with piezoelectric generators or coil-magnet electromagnetic systems. In this regard, [4] found that the inviscid component of the fluid is responsible for the instability and that the viscous drag has a dual influence on energy harvesting. In particular, at a given flow speed, its dissipative action reduces the power output while leading to a sustained limit cycle of oscillations. Molino-Minero-Re et al. [5] examined the energy harvesting performance of different cylinder sizes. The results show that the frequency of oscillation decreases as the diameter of the cylinders increases, whereas the power supplied does not follow a clear trend. Also Abdelkefi et al. [6] focused on the motion of a rigid cylinder, providing a mathematical model that accounts for the coupled lifting force, the movement of the cylinder, and the harvested voltage, describing the lift with a modified van der Pol equation. As a result, the influence of the load resistance of the coupled circuit influences the onset synchronisation, shifting it to higher free-stream velocities. As Abdelkefi et al. [6] stated, Mehmood et al. [7] found the same results regarding the effects of the load of the coupled electromechanical circuit. Andrianne et al. [8] developed an energy harvester based on the phenomenon of wind galloping. More recently, Zhu et al. [9] introduced a new perspective in the field of energy harvesting research by proposing a particular configuration with a circular cylinder combined with a free-rotating pentagram impeller. Cylinder vibration and impeller rotation energy are harvested simultaneously. The result shows an efficiency of 22.6% and an expected power output of 885.53 W/m^3. Finally, Nitti et al. [10] studied the coupling mechanism between cross-flow translation and rotation, providing a single degree of freedom cylinder system. The research findings underlined that the rotation maintains the lock-in condition.

Despite the extensive numerical and experimental contributions inherent in the research and development of VIV devices, no investigations have provided detailed and precise design criteria that can be considered valid for maximising the exploitation of the water-fluid dynamics. In particular, literature contributions typically focus on specific configurations, frequently offering laboratory testing, with few hints about the influence of the flow field conditions on the choice of the design parameters such as mass and control circuit settings (i.e., stiffness and damping).

The present research investigates in detail the mutual relationship between fluid dynamics and body behaviour and attempts to offer design guidelines for a VIV energy harvester, with the aim of maximising the energy production by ensuring the lock-in condition. For this purpose, a database of configurations is considered and virtually analysed under different fluid-dynamic operating conditions using Computational Fluid Dynamics (CFD) tools. In this preliminary investigation, only a basic cross-flow cylinder arrangement is addressed, and the influence of the control system mass and stiffness on the device displacements depending on the flow characteristics is explored, the latter being unambiguously connected to electrical power generation.

The rest of the work is organised as follows. Section 2. describes the model and its validation procedure, while Section 3. presents the results of the analysis. Finally, Section 4. makes conclusive remarks.

2. Model description and validation

The configuration, investigated in this study, is represented by a cross-flow cylinder arrangement, whose behaviour under different water flow conditions was thoroughly analysed to establish the basis for an innovative design strategy aimed at maximising energy production. In this Section, the mathematical description of the mechanical model of the device is first presented. Then, the numerical CFD model and its validation are outlined.

2.1. Mechanical model description

The interaction between the flow stream and the cylinder displacement was modelled by a 2D model concerning an elastically mounted circular cylinder immersed in a cross-flow. The cylinder can undergo vertical displacement; therefore, the single degree-of-freedom system is governed by a forced second-order oscillator equation.

$$m\ddot{\tilde{y}} + c\dot{\tilde{y}} + k\tilde{y} = F_y \tag{1}$$

where F_y is the resulting lift force on the surface of the cylinder, m is the mass of the cylinder, while c and k are the damping and stiffness parameters, respectively. $\tilde{y}$, $\dot{\tilde{y}}$ and $\ddot{\tilde{y}}$ denote vertical dimensional movement, velocity, and acceleration. Since the aim of the study is to propose a design strategy not customised to specific conditions, Eq. (1) was transformed into an equivalent nondimensional formulation by casting $y = \tilde{y}/D$ and $t = \tilde{t}U_\infty/D$, being D the diameter of the cylinder, U_∞ the free stream speed of the flow and $\tilde{t}$ the dimensional time. Thus, the following equation holds:

$$\rho d\ddot{y} + \mu\dot{y} + \xi y = 2c_y \tag{2}$$

https://doi.org/10.52202/069564-0052

where $\rho = \rho_s/\rho_\infty$ is the solid-to-fluid density ratio, $d = A/D^2$ is a geometric parameter in which A is the cylinder area, $c_y = F_y/q_\infty$ is the lift coefficient, with $q_\infty = 1/2\rho_\infty U_\infty^2 D$ the free stream pressure load, while $\mu = c/(\rho_\infty U_\infty D)$ and $\xi = k/(\rho_\infty U_\infty^2)$ are the nondimensional damping and stiffness, respectively.

Equation (2) highlights the relevant design criteria for the system. In particular, body motion is affected by the density ratio (ρ), the geometrical characteristic of the body (d) and the nondimensional damping and stiffness (μ, ξ). However, it is also affected by the lift coefficient (c_y), which in turn depends on the interaction between the fluid motion and the cylinder itself. So, to establish the above-mentioned design parameters, it is necessary to define the fluid-dynamics around the cylinder, but this fluid-dynamics can be only determined once the geometry is defined.

To face this challenge by providing useful design guidelines, it is hence necessary to combine the mechanical model with a CFD 2D model, described in the next section, allowing one to determine the fluid-dynamics for a given geometry.

2.2. CFD simulation settings and model validation

To describe the dynamics of the system within a fluid force field, in this study, the numerical model of the cylinder was built in such a way that it can be free to move vertically. In particular, the ANSYS Fluent platform is used to fill the CFD database. The software, in particular, is specifically used to solve the fluid equation of motion, while Python scripts are employed to postprocess the results.

To analyse the behaviour of the cylinder under free flow conditions, the two-dimensional model consists of a rectangular box of size $(50 \times 30)D$, where D indicates the diameter of the cylinder, in which the cylinder is set at $15D$ from the inlet and is subtracted from the entire fluid domain using a Boolean operation to form a solid part (Figure 1).

Regarding the boundary conditions, the *velocity inlet*, which is a known parameter in the design procedure, is imposed on the left side of the domain to obtain a precomputed free stream Reynolds number, $Re = \rho_\infty u_\infty D/\mu_\infty$. A *wall-type* boundary is enforced at the edge of the cylinder, resulting in a non-slip condition for the velocity components. The upper and lower edges correspond to a *symmetry* condition, and the right domain side imposed a homogeneous pressure distribution according to the *pressure outlet* Fluent option.

The initial dynamics is predicted through *hybrid initialisation*, which implies the solution of simplified equations during ten iterations.

Regarding the pressure-velocity coupling algorithm, the recommendations of the ANSYS Fluent user guide have been followed, and the *PISO* algorithm is used. The method provides stable calculations despite a more significant time step and optimal under-relaxation factor for both momentum and pressure. Default options are used. The discretisation process of the spatial terms accounts for second-order upwind formulas.

The system dynamics is simulated according to a RANS approach in both steady and unsteady versions.

In order to identify the most appropriate numerical model to reproduce most of the critical flow properties of the investigated geometry, the turbulence model and the mesh refinement level are defined by comparison with experimental results and validated numerical results.

Regarding mesh size, three hybrid meshes with increasingly refined dimensions with a size of approximately 20k, 40k, and 90k elements are used. The grids will be referred to as coarse (C), medium (M), and fine (F). In all the three cases, the meshing process has been performed with the built-in meshing software available in ANSYS. A hybrid structured/unstructured approach is used to ensure a reasonable approximation near the cylinder wall region and, simultaneously, reduce the calculation time.

Figure 1 provides a mesh overview and some zooms around the cylinder region for the fine grid of 90k elements. In particular, structured cells are located in the near-wall area (Figure 1c) to capture velocity gradients in the boundary layers. Construction lines are also used to cluster most of the computational cells in the wake region and around the cylinder. The entire meshes are built on the basis of the maximum investigated Reynolds number, i.e. $Re = 10^6$, and keeping the wall Y plus distribution, $y_w^+ = \rho_w u_\tau y_w/\mu_w$, below the unit. This ensures that a sufficient number of cells are used to resolve the near-wall velocity gradients throughout the Reynolds spectrum. Note that ρ_w and μ_w are the wall fluid density and molecular viscosity, y_w is the first-off-the-wall cell distance, while $u_\tau = \sqrt{\tau_w/\rho_w}$ denotes the wall friction velocity, with $\tau_w = \mu_w \partial u_p/\partial y$ the wall shear stress.

Regarding turbulence models, three increasingly sophisticated models are considered: the one equation Spalart-Allmaras (SA) model by Spalart and Allmaras [11], the two equations k-ω Shear Stress Transport (SST) model by Menter [12] and the four equations Transition SST (TSST) model by Menter et al. [13]. The convergence of the flow under steady conditions was monitored, granting 10^{-6} residual drop tolerance of all flow parameters.

https://doi.org/10.52202/069564-0052

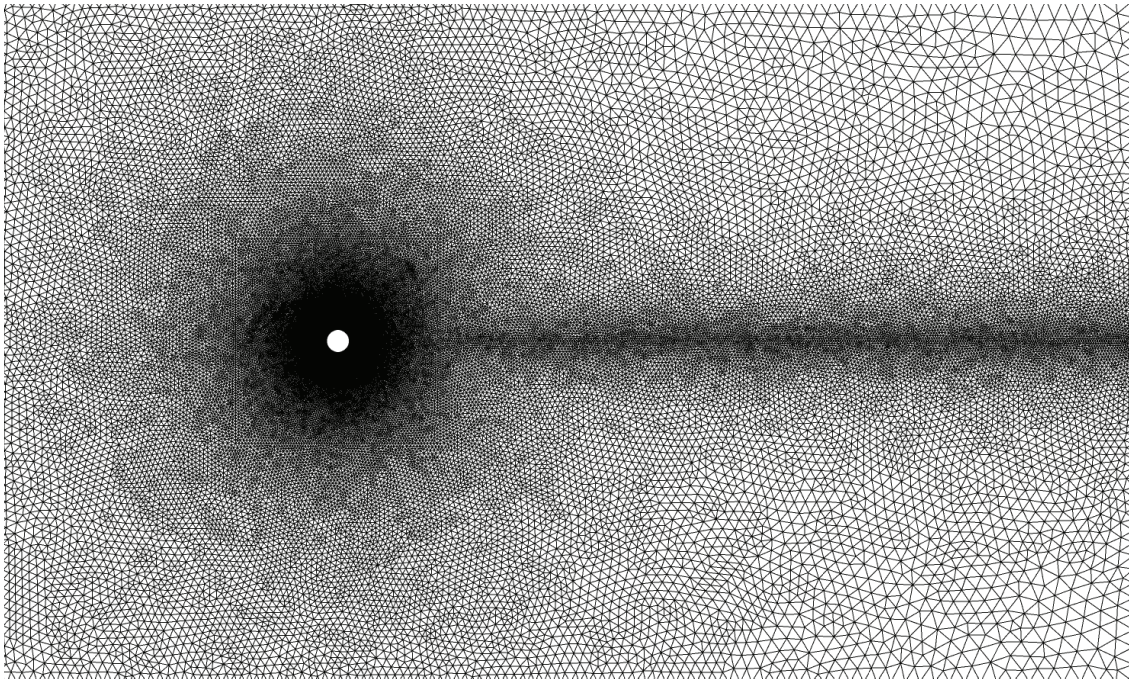

(a) Mesh overview

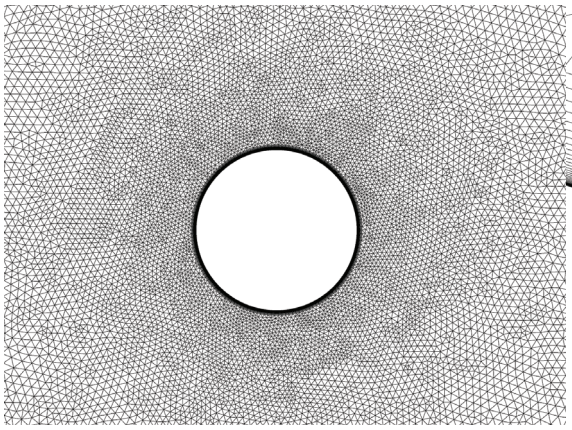

(b) Near cylinder details

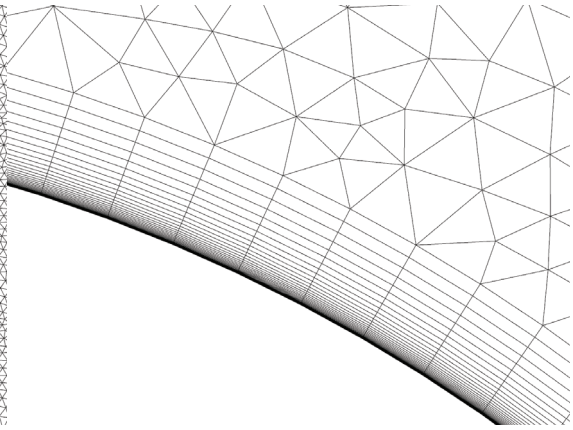

(c) Near wall details

Figure 1: Mesh overview (a) and details (b,c). The figures refers to the fine grid of 90k elements.

To define the most suitable numerical approach, according to the best CFD practises (see, e.g., [14]), the three sets of meshes and the three turbulence models are compared in terms of the cylinder drag coefficient, $C_D = D/q_\infty$, with the experimental results by Warschauer and Leene [15] and with the time average drag value of the unsteady RANS simulations by Ong and Wallace [16] (Figure 2). D denotes the drag force per unit length. In all cases, the Reynolds number of the flow is set to 10^6, which is the maximum Reynolds number that will be used in the following analyses.

As can be seen in Figure 2, the medium and fine arrangements yield little discrepancies, both in the steady- and time-averaged versions of the drag coefficient. A C_D error of around 5% is observed for steady setup, while a 0.4% mismatch is observed in medium arrangements combined with the k-ω SST model.

The results suggest that the medium mesh gives a good compromise between computational performance and accuracy, while adopting the fine mesh would increase the computational time of the simulation drastically, particularly with respect to the unsteady setup, without introducing appreciable accuracy effects.

To fully validate the numerical model, the proper resolution of the boundary layer gradients is also verified. In this regard, we focus on the y_w^+ distribution on the cylinder. Figure 3 shows the y_w^+ distribution as a function of

https://doi.org/10.52202/069564-0052

the angular cylinder coordinate, of the mesh refinement and the turbulence model.

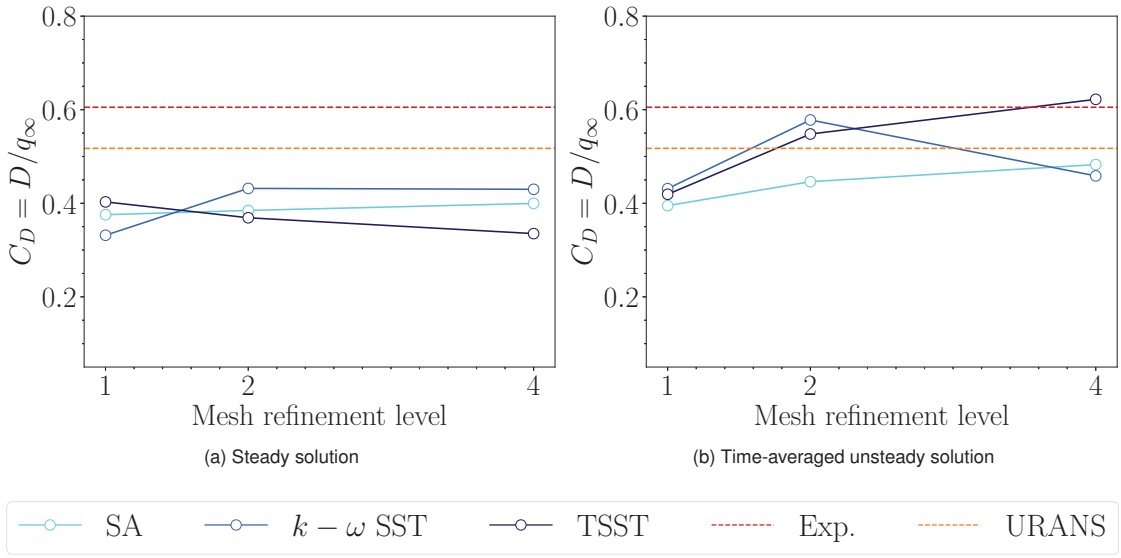

Figure 2: Comparison between cylinder drag coefficient at Re=10^6 as a function of turbulence model and mesh refinement level. Results are compared with the time average drag value of the unsteady RANS simulations by Ong and Wallace [16] and the experimental results by Warschauer and Leene [15].

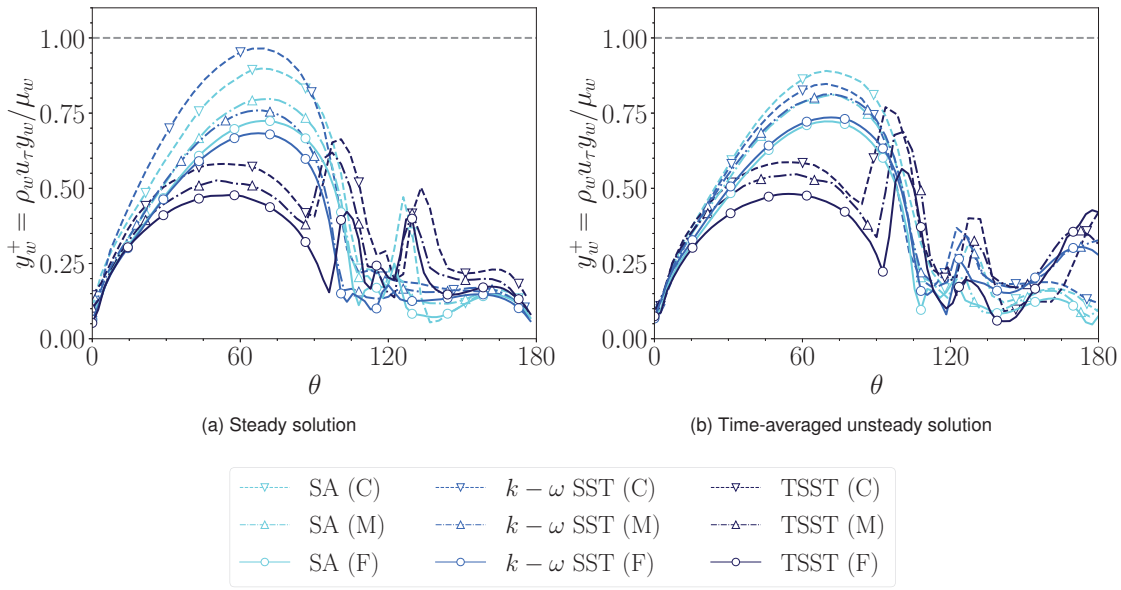

Figure 3: y_w^+ distribution on the upper half of the cylinder as a function of the mesh refinement level and the turbulence model.

Both time-averaged unsteady case (Fig. 3a) and steady results are provided (Fig. 3b). Note that all the built meshes provide results close to the suggested threshold for wall-resolved RANS simulations, i.e., $y_w^+ \leq 1$, giving an average Y plus value around the cylinder from $y_w^+ = 0.46$ for the coarse mesh to $y_w^+ = 0.33$ for the fine setup. Thus, this result confirms that the proposed numerical model provides a good representation of

the velocity profiles near the cylinder surface. Discrepancies between distributions have to be ascribed to turbulence modeling only.

2.3. The database

VIV components can generate a significant amount of energy only when their fundamental frequency matches the natural frequency of the rigid system in a vacuum environment, a condition known as the lock-in state. To characterise the system the non-dimensional parameters are: *(i)* the Strouhal number associated with the body motion, $St_y = f_y D/U_\infty$, where f_y denotes the first harmonic frequency associated with the body motion in the flow, *(ii)* and the Strouhal number of the flow, $St_v = f_v D/U_\infty$, where f_v denotes the frequency associated with the vortex shedding. This system nondimensional dynamics is conveniently described as a function of the so-called reduced velocity, $U_r = U_\infty/(f_n D)$, representing the relationship between the convective time scale of the flow, U_∞/D, and the natural time scale of the motion of the body in a vacuum environment, $1/f_n$, being $f_n = 1/(2\pi)\sqrt{k/m}$ the natural frequency of the cylinder.

The lock-in state is achieved when $St_y \approx 1/U_r$. On the contrary, outside of the lock-in state, body movement tends to follow the vortex shedding frequency, that is, $St_y \approx St_v$.

According to Equation (2), the system dynamics depends on the design parameters but also on the fluid-body interaction, and hence, to choose the design parameters it is necessary to know beforehand the fluid-dynamic behaviour.

To solve this problem, a database of numerical CFD simulations is created, by determining the fluid-cylinder interaction for different values of the diameter of the cylinder D, of the density ratio, of the control stiffness, of the water velocity, and of the Reynolds number.

The resulting database was then organised as follows. Given a certain geometry, the dynamics of the system was parametrically organised to the density ratio and the nondimensional stiffness, setting for simplicity μ equal to zero. However, since ξ depends on the Reynolds regime of the flow, the results are given as a function of the following modified stiffness:

$$k^* = \frac{kD}{mg} \tag{3}$$

where mg is a reference force, with g denoting gravity acceleration. Obviously, ξ is linked to k^* as follows:

$$\xi = k^* \frac{mg}{\rho_\infty U_\infty^2 D} \tag{4}$$

These organised results will be presented in the following section together with an insight of the fluid dynamics in the lock-in state.

3. Results and discussion

3.1. The fluid mechanics of the system in the lock-in condition

As a first step, we analyse fluid mechanics of the system in lock-in condition. Figure 4 shows the non-dimensional vorticity contours as a function of the cylinder location in a lock-in state. The results refer to $Re = 4 \cdot 10^3$, $\rho = 10$ and $k^* = 6.5$. In particular, Fig. 4a shows the location of $y \simeq 0$ in a negative speed framework, $\dot{y} < 0$. Fig. 4b shows the cylinder flow field around its minimal excursion ($y \simeq y_{min}$, $\dot{y} \simeq 0$). Fig. 4c provides the location of the $y \simeq 0$ cylinder in a positive speed framework, $\dot{y} > 0$). Finally, Fig. 4d shows the flow field where the cylinder reaches the dead top location ($y \simeq y_{max}$, $\dot{y} \simeq 0$).

https://doi.org/10.52202/069564-0052

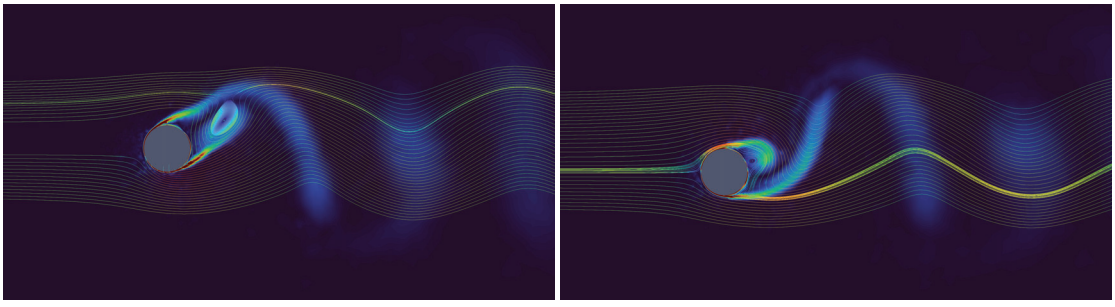

(a) $y \simeq 0, \dot{y} < 0$ (b) $y \simeq y_{min}, \dot{y} \simeq 0$

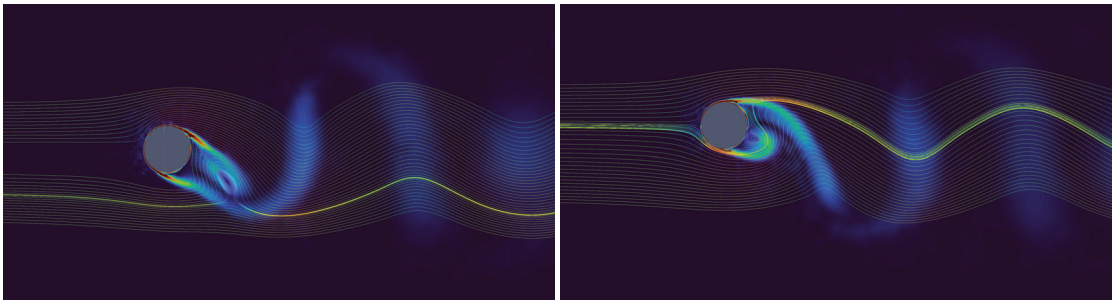

(c) $y \simeq 0, \dot{y} > 0$ (d) $y \simeq y_{max}, \dot{y} \simeq 0$

Figure 4: Instantaneous ω_z vorticity contours and pathlines in four dynamical locations of the cylinder. Present results refers to $Re = 4 \cdot 10^3$, $\rho = 10$ and $k^* = 6.5$.

According to Guilmineau and Queutey [17], the lock-in state is maintained by a vortex pattern near the tail of the cylinder. In particular, the main vortex of the cylinder determines the location of the lower pressure, the value of which is significantly related to the act of motion of the cylinder. The lower and upper dead locations (Fig. 4b and Fig. 4d) indicate that the vortex is quite close to the surface of the cylinder. This state significantly desymmetrises the force field surrounding the cylinder, which is pushed back to the side opposite the tail vortex. The states in which the cylinder passes through the zero displacement location (Figs. 4a and 4c), on the other hand, indicate how the main vortex detaches the surface, allowing the cylinder motion to reach maximum speed.

3.2. Design guidelines and energy production

This section aims to understand the interaction between the frequency of the body motion and the natural frequency of the cylinder when ρ and k^* change in light of the optimisation of the mechanics and fluid dynamics of the system. Indeed, as explained above, the lock-in state is not obvious as a priority, preventing the adoption of a simple and straightforward design procedure. Figure 5 shows the trend of the Strouhal number associated with body movement, St_y, as a function of the reduced speed, U_r, parametrically with respect to the density ratio (Fig. 5a), setting the modified stiffness at 6.5, and the modified stiffness (Fig. 5b), setting the density ratio at 10.

https://doi.org/10.52202/069564-0052

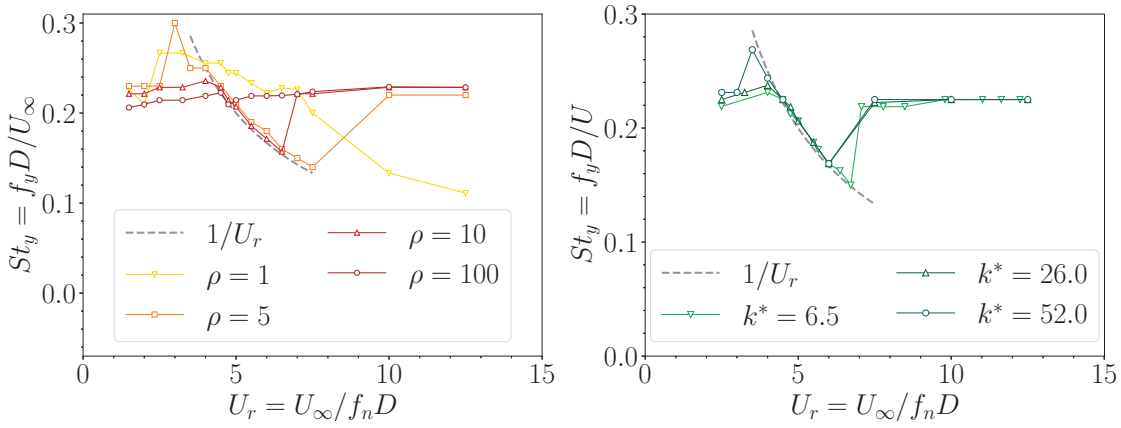

(a) Density ratio effect

(b) Reduced frequency effect

Figure 5: Strouhal number of the body motion as a function of the reduced velocity. Results are reported parametrically to (a) the solid-to-fluid density ratio, fixing $k^* = 6.5$ and (b) the reduced stiffness with $\rho = 10$.

As already explained above, the reduced speed U_r is an excellent self-similarity coordinate since it can be used to compare the convective time with the natural oscillation scale of the cylinder: for certain conditions, as the physical speed increases, a variation in ρ or k^* keeps the curves collapsing in the same intervals. Furthermore, such a representation is extremely useful, as it highlights the lock-in region (grey-shaded branch of the hyperbola in Figure 5).

In Figure 5a, the dynamics of the system is explored with a density ratio of $\rho = \{1, 10, 100\}^T$. The lock-in regime fails for both small and large density ratios. In particular, the $\rho = 1$ arrangement lacks a real lock-in state, and the system tends to a hyperbolic trend but with a systematic error; this indicates that the cylinder oscillates at a frequency primarily determined by the flow, and in general, it is difficult to control. Conversely, high density ratios make the lock-in area mostly disappear, collapsing in a narrow range of reduced speed values. As a result, it is evident that ρ must be kept within a reasonable range, restricting the choice of the VIV material in certain ranges of density, which can be optimised for the specific characteristic of the fluid flow.

In Figure 5b, the analysis is carried out by adjusting ρ to 10 and varying the reduced stiffness within the sample $k^* = \{6.5, 26, 52\}^T$. On the contrary to the density ratio, the stiffness variation preserves the lock-in regime, which always occurs in the same range of reduced velocity, suggesting the existence of an optimal value of the cylinder diameter depending on the fluid velocity.

After grasping the effect of density and stiffness on the lock-in condition, it is also interesting to analyse the system response in terms of displacement in this condition and outside. This analysis is of fundamental importance, as the nondimensional root mean square displacement of the cylinder, y_{rms}/D, is directly related to the amount of energy that the VIV system can extract from the flow.

Figure 6 shows the y_{rms}/D trend as a function of the reduced speed (Fig. 6a) and of the Reynolds number of the flow (Fig. 6b). Data are provided parametrically to the density ratio ρ, with a fixed reduced stiffness of $k^* = 6.5$.

All curves exhibit bumped-like behaviour, clustering non-trivial cylinder displacements in the $U_r = 3 \div 10$ range.

The reduced speed at which the highest displacement is centred is essentially independent of the density ratio and is limited to a band around $U_r \approx 5$, in agreement with the results presented in Figure 5a. On the other hand, the extension of the bump is heavily affected by ρ, and the lower ρ, the higher the operating range of the VIV device.

Analysing the simulation results as a function of the Reynolds number, significant insights can be derived in terms of the flow regime in which the device is supposed to be installed. In fact, as ρ increases, the peak of the displacement moves to a lower Reynolds regime. This is an important information at the design level since it highlights that the higher the device mass with respect to the flow, the lower the Reynolds number tolerated in the system.

In conclusion, the density ratio is a very tricky design parameter, since as ρ increases, the operational range of the lock-in state narrows dramatically, thus reducing the flexibility of the VIV device, but also requires higher Reynolds, which are not so easy to reach in the water flows targeted by the VIV device. Therefore, keeping ρ in

https://doi.org/10.52202/069564-0052

the range of 10 seems to represent a good compromise between flexibility and applicability, in the hypothesis of reduced stiffness of 6.5.

To verify the influence of reduced stiffness k^* on these conclusions, the results were analysed, fixing the density ratio equal to 10 and varying the reduced stiffness. Figure 7 shows the y_{rms}/D trend as a function of the reduced speed (Fig. 7a) and the Reynolds number of the flow (Fig. 7b).

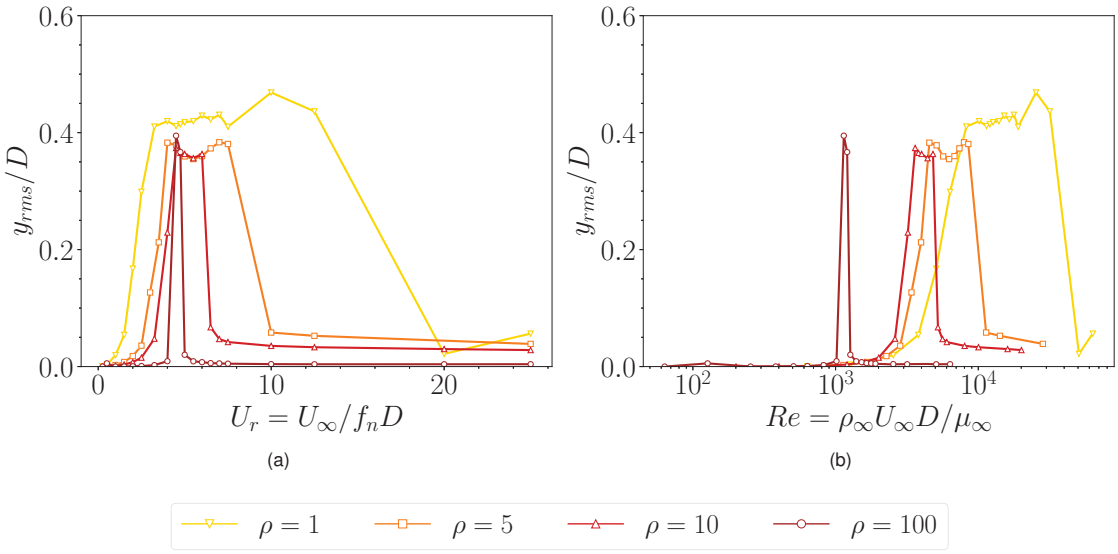

Figure 6: Density ratio effect on the non-dimensional root-mean-square cylinder displacement as a function of (a) the reduced velocity and (b) the flow Reynolds number. Present results are obtained with a reduced stiffness equal to k^* = 6.5.

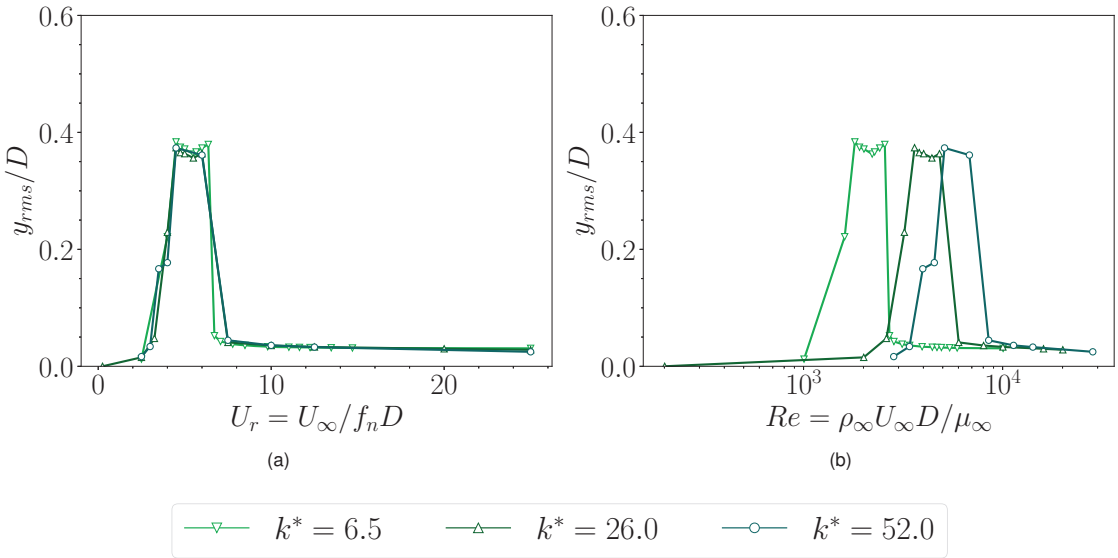

Figure 7: Reduced stiffness effect on the non-dimensional root-mean-square cylinder displacement as a function of (a) the reduced velocity and (b) the flow Reynolds number. Present results are obtained with a density ratio equal to ρ = 10.

https://doi.org/10.52202/069564-0052

It can be seen that the reduced stiffness keeps the displacement amplitude constant as a function of the Reynolds regime without narrowing or widening the lock-in region (Fig. 7b). Subsequently, in terms of reduced velocity (Fig. 7a), this causes the system lock-in in the same U_r range, clustered around 5. Therefore, another important design guideline for VIV devices can be deduced: controlling the stiffness of the system is the key to match the lock-in condition (and hence the maximum displacement) with the flow regime of the installation site.

Note that in the lock-in state, the cylinder oscillates with mean square displacements of $\approx 0.4D$ (Fig. 7); thus performing harmonic oscillations of amplitude $\approx 0.4\sqrt{(2)}D$. This result is independent of the Reynolds regime and of the mechanical characteristics of the system, which is a really interesting starting point for the preliminary design of the system.

Finally, it is also possible to estimate the mechanical power that can be extracted by the VIV device in the different configurations (reduced stiffness, density ratio, etc.). In particular, the non-dimensional mechanical power (power coefficient) is determined according to the following equation:

$$P^*_{rms} = \sqrt{\frac{1}{\Delta T}\int_{t+\Delta T}\left[\frac{\dot{y}(t)}{U_\infty}\frac{F_y(t)}{1/2\rho_\infty D U^2_\infty}\right]^2 dt} \tag{5}$$

where $F_y(t)$ and $\dot{y}(t)$ are the instantaneous lift force and cylinder velocity respectively.

Figure 8 shows the trend of the mechanical power coefficient, P^*_{rms}, as a function of the reduced speed and parametrically with the density ratio and the reduced-stiffness.

As shown in Figure 8, P^* is significant only in the lock-in area ($U_r \approx 5$) where values around 0.2 are reached. In particular, if the density ratio increases, the power coefficient decreases (Fig. 8a); while, as the modified stiffness varies, the power output remains practically constant.

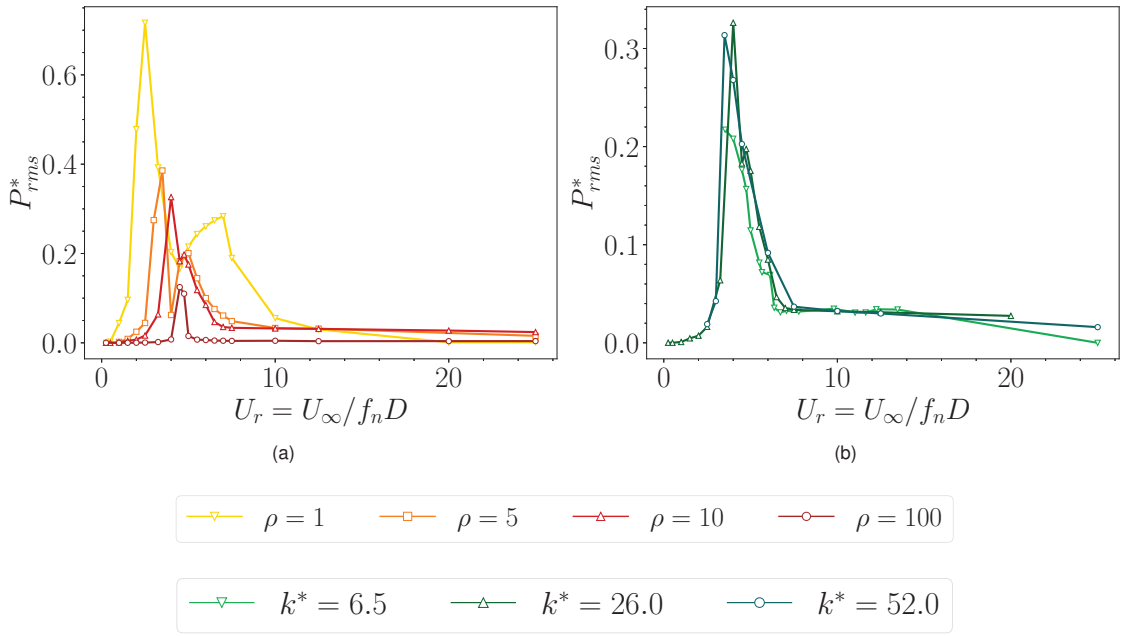

Figure 8: Non-dimensional power coefficient associated to the cylinder body motion as a function of the density ratio, ρ and the reduced stiffness, k^*.

4. Conclusions

The proposed investigation addresses the critical aspects of the design of VIV devices for energy harvesting, with the aim of providing some preliminary design guidelines and estimation of the mechanical power that can be extracted.

In particular, a simple cylinder configuration in cross-flow conditions is investigated and modelled in terms of mass, damping, and stiffness. This model was combined with a numerical CFD model to estimate the

https://doi.org/10.52202/069564-0052

fluid-body interaction. By means of these models, the system behaviour was investigated in several configurations, by parametrically varying the system fundamental mechanical properties (solid-to-fluid density ratio and stiffness of the control system), the cylinder geometry (diameter), and the flow regime in which it is immersed.

The resulting database was analysed to highlight the influence of the different parameters on the achievement of the lock-in conditions, which results to be achieved for a reduced velocity value of about 5.

The analysis also revealed that the density ratio is a key design parameter, since the functional properties of the VIV device are ensured only for modest values of it, roughly around 10. Smaller values of the density ratio make the system lose its ability to attain the lock-in state by creating a difficult-to-control oscillation pattern with optimal Reynolds values between 10^4 and 10^5. On the other hand, high density ratio values dramatically shrink the lock-in zone, limiting the flexibility of the VIV device to maintain lock-in conditions even in operating conditions close to the optimal one.

Concerning the stiffness effects, this well fits the system modulation, especially to match the maximum displacements on a specific Reynolds regime. In fact, if the density ratio is kept constant, the control system stiffness can retain the cylinder displacements and lock-in state at different Reynolds regimes.

Future analyses will investigate a broader spectrum of density ratios and reduced stiffness to build an extensive database in view of system sizing. The damping effect and other geometrical configurations will also be analysed to further investigate the VIV devices behaviour and their best design practises.

Acknowledgments

This study is founded by the European Union. The project has received funding from the European Climate, Infrastructure and Environment Executive Agency research and innovation programme under grant agreement number 101084362. However, the views and opinions expressed are those of the authors alone and do not necessarily reflect those of the European Union. Neither the European Union nor the granting authority can be held responsible for them. The authors also acknowledge the CINECA award under the ISCRA initiative, for the availability of high-performance computing resources with the project H-HOPE1 HP10CGZTU8.

Abbreviations

CFD Computational Fluid Dynamics

RANS Reynolds-Averaged Navier-Stokes

SA Spalart-Allmarass

SST Shear Stress Transport

TSST Transition Shear Stress Transport

VIV Vortex-Induced Vibration

References

[1] Indranil Goswami, Robert H Scanlan, and Nicholas P Jones. Vortex-induced vibration of circular cylinders. i: experimental data. *Journal of Engineering Mechanics*, 119(11):2270–2287, 1993. doi: https://doi.org/10.1061/(ASCE)0733-9399(1993)119:11(2270).

[2] Hugh Blackburn and Ron Henderson. Lock-in behavior in simulated vortex-induced vibration. *Experimental Thermal and Fluid Science*, 12(2):184–189, 1996. doi: https://doi.org/10.1016/0894-1777(95)00093-3.

[3] Ming Zhao, Kalyani Kaja, Yang Xiang, and Guirong Yan. Vortex-induced vibration (VIV) of a circular cylinder in combined steady and oscillatory flow. *Ocean Engineering*, 73:83–95, 2013. doi: https://doi.org/10.1016/j.oceaneng.2013.08.006.

[4] Kiran Singh, Sébastien Michelin, and Emmanuel De Langre. Energy harvesting from axial fluid-elastic instabilities of a cylinder. *Journal of Fluids and Structures*, 30:159–172, 2012. doi: https://doi.org/10.1016/j.jfluidstructs.2012.01.008.

[5] Erik Molino-Minero-Re, Montserrat Carbonell-Ventura, Carles Fisac-Fuentes, Antoni Mànuel-Làzaro, and Daniel Mihai Toma. Piezoelectric energy harvesting from induced vortex in water flow. In *2012 IEEE International Instrumentation and Measurement Technology Conference Proceedings*, pages 624–627. IEEE, 2012. doi: https://doi.org/10.1109/I2MTC.2012.6229686.

[6] A Abdelkefi, MR Hajj, and AH Nayfeh. Phenomena and modeling of piezoelectric energy harvesting from freely oscillating cylinders. *Nonlinear Dynamics*, 70(2):1377–1388, 2012. doi: https://doi.org/10.1007/s11071-012-0540-x.

[7] A Mehmood, A Abdelkefi, MR Hajj, AH Nayfeh, I Akhtar, and AO Nuhait. Piezoelectric energy harvesting from vortex-induced vibrations of circular cylinder. *Journal of Sound and Vibration*, 332(19):4656–4667, 2013. doi: https://doi.org/10.1016/j.jsv.2013.03.033.

[8] Thomas Andrianne, Renar P Aryoputro, Philippe Laurent, Gérald Colson, Xavier Amandolese, and Pascal Hémon. Energy harvesting from different aeroelastic instabilities of a square cylinder. *Journal of Wind Engineering and Industrial Aerodynamics*, 172:164–169, 2018. doi: https://doi.org/10.1016/j.jweia.2017.10.031.

[9] Hongjun Zhu, Ying Zhao, and Tongming Zhou. Cfd analysis of energy harvesting from flow induced vibration of a circular cylinder with an attached free-to-rotate pentagram impeller. *Applied energy*, 212:304–321, 2018. doi: https://doi.org/10.1016/j.apenergy.2017.12.059.

[10] A Nitti, G De Cillis, and MD de Tullio. Cross-flow oscillations of a circular cylinder with mechanically coupled rotation. *Journal of Fluid Mechanics*, 943, 2022. doi: https://doi.org/10.1017/jfm.2022.442.

[11] Philippe Spalart and Steven Allmaras. A one-equation turbulence model for aerodynamic flows. *AIAA*, 439, 01 1992. doi: 10.2514/6.1992-439.

[12] F. Menter. Two-equation eddy-viscosity turbulence models for engineering applications. *AIAA Journal*, 32:1598–1605, 01 1994. doi: https://doi.org/10.2514/3.12149.

[13] Florian Menter, RB Langtry, S. Likki, Y. Suzen, P. Huang, and S Völker. A correlation-based transition model using local variables-part I: model formulation. *Journal of Turbomachinery*, 128, 07 2006. doi: 10.1115/1.2184352.

[14] Francesco De Vanna, Danilo Bof, and Ernesto Benini. Multi-objective rans aerodynamic optimization of a hypersonic intake ramp at mach 5. *Energies*, 15(8):2811, 2022. doi: https://doi.org/10.3390/en15082811.

[15] K.A. Warschauer and J.A. Leene. Experiments on Mean and Fluctuating Pressures of Circular Cylinders at Cross Flow at Very High Reynolds Numbers. *Proceeding of International Conference on Wind Effects on Buildings and Structures*, pages 305–315, 1971.

[16] Lawrence Ong and J Wallace. The velocity field of the turbulent very near wake of a circular cylinder. *Experiments in fluids*, 20(6):441–453, 1996. doi: https://doi.org/10.1007/BF00189383.

[17] Emmanuel Guilmineau and P Queutey. A numerical simulation of vortex shedding from an oscillating circular cylinder. *Journal of Fluids and Structures*, 16(6):773–794, 2002. doi: https://doi.org/10.1006/jfls.2002.0449.

https://doi.org/10.52202/069564-0052